

1. Measurement error

a. Radiometer diagram

A radiometer comprises four parts. The reflector and antenna collect incoming radiance that enters the feedhorn followed by diplexers or orthomode transducers (OMT) for different channels. When the radiometer operates in the nominal mode, the radiance alternates between the cold-space, warm load, and Earth scenes, as the reflector spins. A ranges of errors can take place in this part as in the diagram and we will detail them shortly.

The receiver front-end is a key part. It comprises a cascade of a low-noise amplifier (LNA), LO if needed, and band-pass filters (BPF) where the incoming radiance gets amplified and filtered. During the process, electronic noise and other factors can affect the radiometer performance.

The receiver back-end is the video amplifying and recording. It has a square-law detector, video amplifier, and analog to digital converter (ADC). After data down-linking, the raw data are processed into level-1 T_A and T_b as well as other science data in the ground data center.

b. Generating count and T_A with noise and orbital oscillation

The receiver processes radiance to count. After calibration, the count is converted to T_A . Noise from RF circuit is accompanied with the process. We developed a receiver module for processing count to T_A with generated noise.

The noise-free count of a radiometer can be written as Ulaby et al. (2014)

$$C = (T_A + T_R)G \quad (1)$$

where C , T_A is antenna temperature, T_R is receiver temperature, G is the power gain. The system temperature can be defined as $T_{sys} = T_A + T_R$. In the presence of noise, it can be written as

$$C = (T_A + T_R + \sum n_i)G \quad (2)$$

where n_i represents a number of aforementioned individual noise, including both additive and signal-dependent noise. The short-term gain fluctuation also results in noise and can be counted as an individual n_i implicitly. The long-term gain oscillation subject to orbital variation is different from short-term fluctuation. It will be introduced in Section of Orbital Oscillation.

The noise term n_i and its generating can be associated with two families of additive and signal-dependent noise. The additive noise is written as ?

$$x = s + n \quad (3)$$

where x is the measurand, s is the signal, n is the additive noise that is signal independent. The additive noise model has mathematical advantages: noise can be generated with many random number generators, and the magnitude can

be easily adjusted. The noise magnitude can be set and adjusted with respect to the channel-dependent NEDT Ulaby et al. (2014).

Thermal noise is due to the random motion of agitated charger carriers Lee (2004); Vasilescu (2005); Schiek et al. (2006). The additive model is used to generate thermal noise. Thermal noise is treated as additive white Gaussian noise (AWGN) and generated with a pseudo random number generator (RNG). The default RNG is the Mersenne Twister and AWGN is assumed to be zero-mean Matsumoto and Nishimura (1998). The noise generating is different in different runs. But in some cases, the same noise needs to be generated for testing the sensitivity of other error sources. This can be realized by fixing the RNG and its seed.

1/f noise is also called flicker noise or excess noise. It can arise from different mechanisms. It is found pronounced in electronics sensitive to surface phenomenon related to charge trapping and releasing and carrier generation and recombination Lee (2004); Vasilescu (2005); Schiek et al. (2006). 1/f noise is produced with Fast Fourier Transform (FFT) Sullivan et al. (1990); Riley (2008). We first generate AWGN in the time domain. FFT transform is applied and multiplied with a term of power-law exponent of -1. The inverse FFT is applied for random numbers back in the time domain

$$\begin{aligned} h(\omega) &= \mathcal{F}(n_{\text{AWGN}}(t)) \\ n(t) &= \mathcal{F}^{-1}(h(\omega)f^\alpha) \end{aligned} \quad (4)$$

where the first equation denotes the Fourier transform of $n_{\text{AWGN}}(t)$, and the second one is the inverse transform with an additional power law term $h(\alpha)f^\alpha$. For 1/f noise, $\alpha = -1$.

Phase and amplitude noise arise with a LO. This is very common for V/W/G bands, as LO performs heterodyning. A category of power-law noise can be produced, including the random walk FM noise ($\alpha = -4$) related to oscillator environment, flicker FM ($\alpha = -3$) from resonance mechanism, white FM ($\alpha = -2$) from resonator frequency standards, flicker PM ($\alpha = -1$) due to noisy electronics, white PM ($\alpha = 0$) from phase noise in stages of amplification Sullivan et al. (1990). The causes of noise are complex in practice and can come from multiple mechanisms. Oscillator noise is generated the same way with the FFT method.

Quantization noise is from ADC with $\alpha = 2$ Sullivan et al. (1990); Schiek et al. (2006). It is also generated with the FFT method. Other power-law noise can also be generated in the simulator based on FFT transform with positive α Riley (2008).

The signal-dependent noise is produced in a different way. Shot noise is due to the discrete nature of charger, and it is Poisson noise that depends on the signal Lee (2004). It is generated with a Poisson RNG as Kuan et al. (1985)

$$n_{\text{shot}} = P_\lambda(T_{\text{sys}}) \quad (5)$$

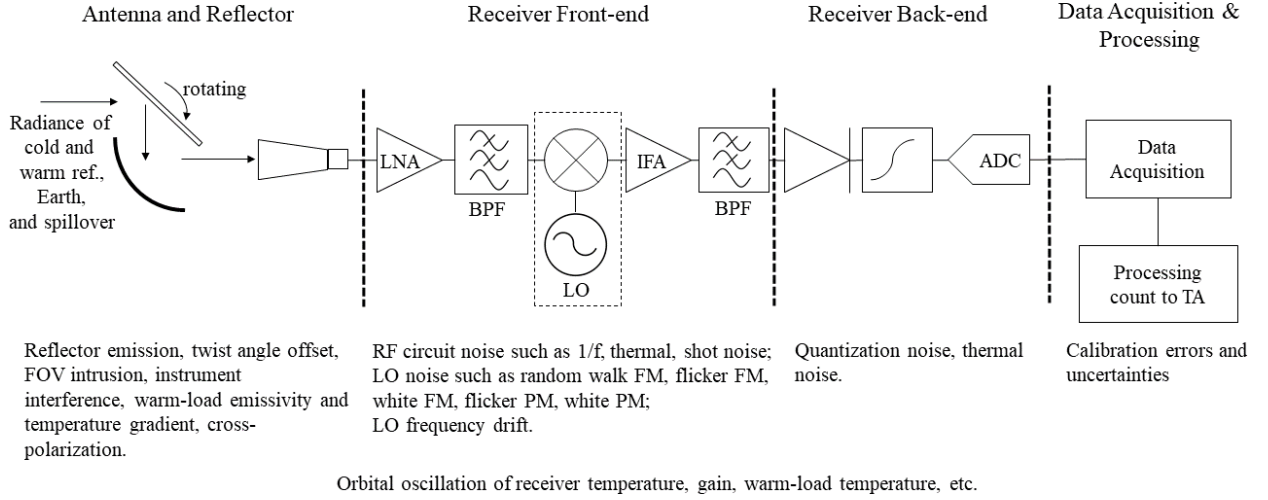


FIG. 1. Diagram of a radiometer with noise and error sources illustrated.

where shot noise is a function of T_{sys} and P_L is the Poisson RNG with λ as the Poisson distribution parameter.

The payload environment usually has an orbital oscillation as the spacecraft orbits the Earth ??????. It is due to the change of solar incidence angle and environment temperature along the orbit. The radiometer gain and warm-load temperature oscillate with a period same as the spacecraft orbital period ?. For MHS, the orbital period is ~ 100 minutes. The orbital oscillation can be described as

$$\begin{aligned} T_W &= T_{W0} + \Delta T_W(t, \lambda, a, \phi) \\ G &= G_0 + \Delta G(t, \lambda, a, \phi) \end{aligned} \quad (6)$$

where T_{W0} and G_0 are constant, and ΔT_W and ΔG are oscillation in terms of waveform as a function of time t , wavelength λ , amplitude a , and phase ϕ . A variety of waveforms can be simulated. We can also import empirical orbital oscillations from observations as the oscillation term. In this study, we use sinusoidal wave with the empirical magnitudes from observation ?.

A radiometer observes both the cold and warm reference targets and the Earth scene during one complete rotation of the reflector. We generate counts as follows

$$\begin{aligned} C_W &= (T_{A,W} + T_R + n_W)G \\ C_C &= (T_{A,C} + T_R + n_C)G \\ C_S &= (T_{A,S} + T_R + n_S)G \end{aligned} \quad (7)$$

where $T_{A,W}$, $T_{A,C}$, and $T_{A,S}$ are the warm-load, cold-space, and Earth scene temperature, respectively. n_W , n_C , and n_S are corresponding noise, and C_C , C_W , C_S are counts. If the warm-load is a perfect blackbody, there is $T_{A,W} = T_W$. And $T_{A,C}$ equals the cosmic temperature T_C , if the cold-space

view has no contamination from the reflector emission or field of view (FOV) intrusion.

The scanning mechanism of a radiometer determines the way of data sampling that should be counted in simulation. Figure 5 shows the diagram of MHS scan. As the reflector spins, the radiance received by the receiver alternates between the cold space, warm load, and Earth views. In between the effective objects, the radiometer is still working but sees the radiometer itself and the data are not usable. MHS has a rotation period of 2.67 seconds with a duty cycle of 68% for viewing Earth and reference targets Robel and Graumann (2014).

The scanning produces data as a conditional sampling with only a portion of data used. The recorded data are discrete chunks with gaps in between, and so is the noise. The conditional sampling has a profound influence. For instance, 1/f noise has a non-stationary mean that changes with time. The 68% duty cycle means longer time ($1/0.68$) and larger variability for the same amount of data with 1/f noise compared to that without gaps. In addition, the discrete data with gaps can result in a difference between population statistics and sample statistics. Our simulator counts the scanning and sampling.

We simulate the null count of the other 35% measuring time as

$$C_N = (T_{A,N} + T_R + n_N)G \quad (8)$$

where C_N , $T_{A,N}$, and n_N denote the null count, scene temperature, and noise, respectively. The null simulation is not used but better represents MHS work mode of a conditional sampling.

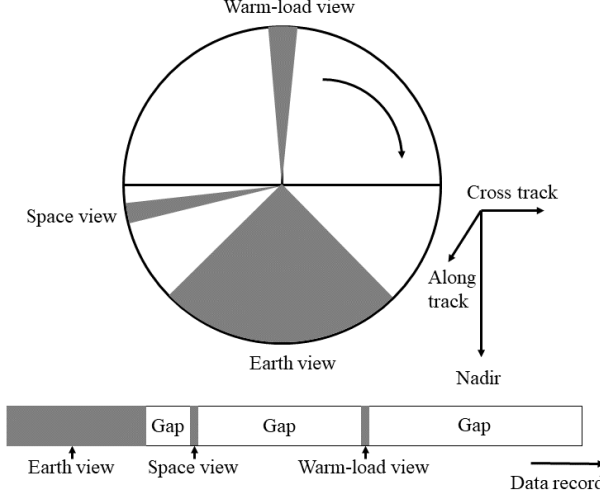


FIG. 2. The scanning mechanism of MHS. In the nominal operating, the receiver sees the Earth, cold space, and warm load in turn with gaps in between as the reflector rotates. The duty cycle of the effective target views is about 68%. The data records are discrete chunks in time series, which is a conditional sampling. The data streaming is counted in the simulator.

After generating count for scene, cold and warm references, T_A is calculated

$$T_{a,s} = \frac{(T_w - T_c)}{(C_w - C_c)}(C_s - C_c) + T_c \quad (9)$$

where $T_{a,s}$ is the scene temperature, T_w for warm load temperature, T_c is cold space temperature. C_w , C_c , C_s are count for warm load, cold space, and scene respectively.

If nonlinearity is considered, there is ATB (2016)

$$T'_{a,s} = T_{a,s} + 4T_n \frac{(C_s - C_c)}{(C_w - C_c)} \left[1 - \frac{(C_s - C_c)}{(C_w - C_c)} \right] \quad (10)$$

where $T'_{a,s}$ is after nonlinear correction, $T_{a,s}$ is from linear calibration, T_n is the term of peak nonlinearity that is often a look-up table from prelaunch test.

Examples of generated noise are shown in Figure 3. It is seen that noise can exhibit different characteristics in the time and frequency domain. For noise like 1/f noise, a distinct feature is that its mean is non-stationary with time. The same is true for its variance. This is different from thermal noise, which has a stationary mean and variance that is time invariant. These different noise can be set in a flexible way. Their magnitudes can be adjusted to the channel NEDT. They can be combined and blended with varying percentages. This is very useful to diagnose their characteristics and differentiate them.

c. Windowing, calibration

This section present details of windowing and calibration. Windowing is used for smoothing cold-space and

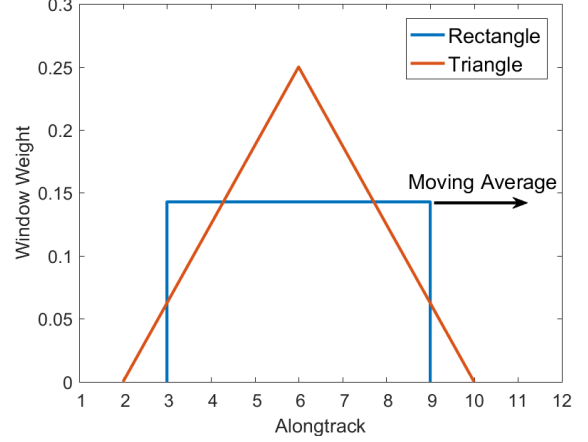


FIG. 3. Examples of rectangular and triangular windows. The windows span a finite along-track length and are used for smoothing radiometer counts in deriving gain and brightness temperature.

warm-load counts. The colds-space counts are smoothed as

$$\overline{C_{Cj}} = \frac{1}{n_{cc}} \sum_{k=j-n_1}^{j+n_2} w_k \sum_{i=1}^{n_{cc}} C_{Ci,j}, \quad (11)$$

where $C_{Ci,j}$ is the cold-space counts as a function of scan positions in terms of cross-track i and along-track j . We refer cross-track measurements as *samples* and along-track measurements as *scans* hereafter. n_{cc} is the number of cross-track samples of cold counts. For example, ATMS and MHS have $n_{cc} = 4$. n_1 and n_2 are related to the window length L through the floor function as

$$n_1 = \lfloor \frac{L-1}{2} \rfloor \quad \text{and} \quad n_2 = \lfloor \frac{L}{2} \rfloor. \quad (12)$$

w_k is a window function with a length of L for smoothing counts along track. w_k can be a rectangular window as

$$w_k = \frac{1}{L}, \quad 0 \leq k \leq L-1. \quad (13)$$

A triangular window is also often used as

$$w_k = \begin{cases} \frac{2}{L+1} \left(1 - \frac{|2k-L+1|}{L+1} \right), & 0 \leq k \leq L-1, \text{ odd } L, \\ \frac{2}{L} \left(1 - \frac{|2k-L+1|}{L} \right), & 0 \leq k \leq L-1, \text{ even } L. \end{cases} \quad (14)$$

A triangular window of $L = 7$ has been used for all MHS and AMSU-A/B at EUMETSAT and NOAA Mo (1996); Weng et al. (2013); ?; ?); Robel and Graumann (2014).

Likewise, $C_{Wi,j}$ is smoothed

$$\overline{C_{Wj}} = \frac{1}{n_{cw}} \sum_{k=j-n_1}^{j+n_2} w_k \sum_{i=1}^{n_{cw}} C_{Wi,j}, \quad (15)$$

where n_{cw} is the cross-track number of warm-load counts.

The warm-load PRT temperature, from the average of multiple PRTs, is smoothed as

$$\overline{T_{Wj}} = \sum_{k=j-n_1}^{j+n_2} w_k T_{Wj}. \quad (16)$$

Then, the power gain $\overline{G_{Sj}}$ is given by

$$\overline{G_j} = \frac{\overline{C_{Wj}} - \overline{C_{Cj}}}{\overline{T_{Wj}} - T_C}, \quad (17)$$

where T_C is the cosmic temperature.

Earth scene antenna temperature is

$$T_{A,Si,j} = \frac{1}{G_j} (C_{Si,j} - \overline{C_{Cj}}) + T_C, \quad 1 \leq i \leq n_{cs}. \quad (18)$$

where n_{cs} is the cross-track number of Earth scene.

In addition to Earth scene, it is useful to derive warm-load and cold-space antenna temperature for determining the Noise Equivalent Delta Temperature (NEDT) and decomposing noise. In contrast to the cold-space counts, we split the cross-track warm-load counts into two subsets for deriving the gain and warm-load antenna temperature $T_{A,W}$. Doing so assures the independency between the derived gain and $T_{A,W}$, avoiding generating a pseudo f^2 in the frequency domain due to the inappropriate signal processing. A pseudo f^2 noise spectrum underestimates 1/f noise since its low-frequency regime is ignored. We suggest reader refer to ? for details.

We first smooth half of cross-track $C_{Wi,j}$ as

$$\overline{C_{Wi,j}} = \frac{2}{n_{cw}} \sum_{k=j-n_1}^{j+n_2} w_k \sum_{i=1}^{\frac{n_{cw}}{2}} C_{Wi,j}, \quad 1 \leq i \leq \frac{n_{cw}}{2}, \quad (19)$$

where n_{cw} is number of cross-track warm counts, which is four for MHS. Then, the power gain $\overline{G_{CWj}}$ is given by

$$\overline{G_{CWj}} = \frac{\overline{C_{Wi,j}} - \overline{C_{Cj}}}{\overline{T_{Wj}} - T_C}, \quad 1 \leq i \leq \frac{n_{cw}}{2}, \quad (20)$$

where T_C is the cosmic temperature.

The other half of cross-track $C_{Wi,j}$ is used for deriving the warm-load antenna temperature $T_{A,W}$

$$T_{A,Wi,j} = \frac{1}{\overline{G_{CWj}}} (C_{Wi,j} - \overline{C_{Cj}}) + T_C, \quad \frac{n_{cw}}{2} + 1 \leq i \leq n_{cw}. \quad (21)$$

d. Decomposing Noise

In the above section, we obtain the cold-space or warm-load antenna temperature. We proceed to derive the noise.

The orbital oscillations is removed with the warm-load PRT

$$\Delta T_{A,Wi,j} = T_{A,Wi,j} - \overline{T_{Wj}}, \quad \frac{n_{cw}}{2} + 1 \leq i \leq n_{cw}, \quad (22)$$

where $\Delta T_{A,W}$ is the warm-load noise.

NEDT is the unbiased second central moment of noise ?

$$\text{NEDT}_{\text{total}} = \sqrt{\frac{1}{MN-1} \sum_{j=1}^N \sum_{i=1}^M (\Delta T_{A,Wi,j} - \overline{\Delta T_{A,W}})^2}, \quad (23)$$

where $\Delta T_{A,W}$ is a $M \times N$ matrix, and $\overline{\Delta T_{A,W}}$ is

$$\overline{\Delta T_{A,W}} = \frac{1}{MN} \sum_{j=1}^N \sum_{i=1}^M \Delta T_{A,Wi,j}. \quad (24)$$

We can break down total noise into thermal and 1/f noise based on their spectra information, since thermal noise dominates on a small time scale while 1/f noise is significant on a large time scale. Thermal noise is calculated as ?

$\text{NEDT}_{\text{thermal}} =$

$$\sqrt{\frac{1}{2N(M-1)} \sum_{j=1}^N \sum_{i=1}^{M-1} (\Delta T_{A,Wi+1,j} - \Delta T_{A,Wi,j})^2}. \quad (25)$$

The above equation calculates the unbiased standard deviation of adjacent cross-track samples of a time scale of a couple of milli-second. The above equation is based on Allan deviation, which is an unbiased estimate of thermal noise that is Gaussian additive white noise ??.

1/f noise is given by

$$\text{NEDT}_{1/f} = \sqrt{(\text{NEDT}_{\text{total}}^2 - \text{NEDT}_{\text{thermal}}^2)}. \quad (26)$$

In the presence of noise other than thermal and 1/f noise, this equation gives the magnitude of non-thermal noise.

The 1/f percentage is defined as ?

$$P_{1/f} = \frac{\text{NEDT}_{1/f}^2}{\text{NEDT}_{\text{total}}^2} \times 100\%. \quad (27)$$

$P_{1/f}$ ranges from 0 to 100%. In ?, the partitioning of thermal and 1/f noise has been validated with simulation and observation. While we have calculated noise of warm-load, the similar procedure can be applied to derive the cold-space noise as well.

e. Cross-pol Contamination

The antenna main polarization (co-pol) sees some radiation leakage from the orthogonal polarization plane

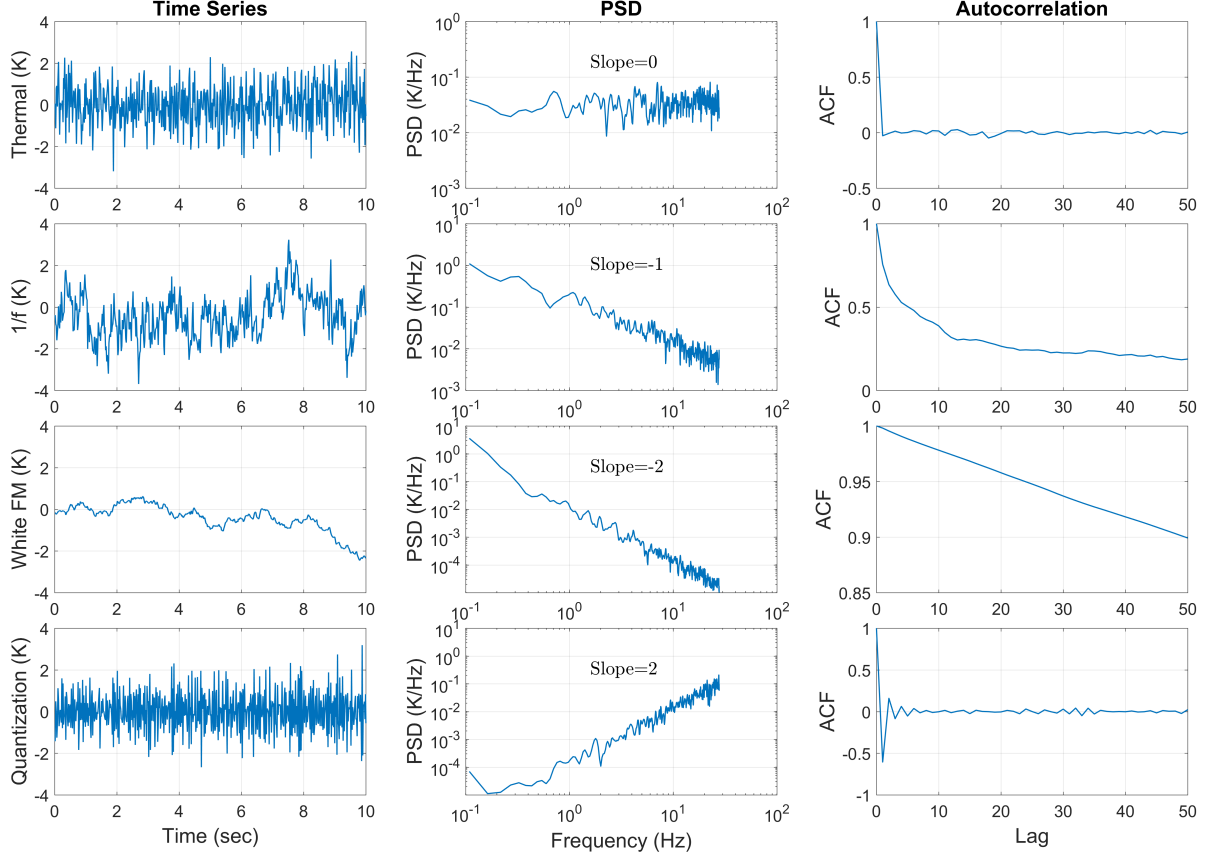


FIG. 4. Examples of simulated noise in time series, power spectrum, and auto-correlation. These include thermal noise, 1/f, white FM, and quantization from up to down, which exhibit different characteristics in the time and frequency domain.

(cross-pol). The cross-pol leakage can be due to the antenna asymmetry, defects, excitation of higher-order modes (Davis and Agarwal (2011)). Cross-pol correction is a necessary step in APC. In the simulator, the cross-pol is a 4×4 matrix as

$$\begin{bmatrix} T'_v \\ T'_h \\ T'_3 \\ T'_4 \end{bmatrix} = \begin{bmatrix} C_{vv} & C_{vh} & C_{v3} & C_{v4} \\ C_{hv} & C_{hh} & C_{h3} & C_{h4} \\ C_{3v} & C_{3h} & C_{33} & C_{34} \\ C_{4v} & C_{4h} & C_{43} & C_{44} \end{bmatrix} \begin{bmatrix} T_v \\ T_h \\ T_3 \\ T_4 \end{bmatrix} \quad (28)$$

where the $C_{i,j}$ is cross-pol coefficients that transforms the cross-pol free Stokes (right) to the new Stokes (left). The values of the coefficients can be customized. In the case of cross-pol free, the matrix is the identity matrix. Examples of cross-pol sensitivity are presented in the results.

f. Twist angle offset

The twist angles refer to a set of reflector and polarization angles that affect radiance and polarization. For a cross-track scanning radiometer like AMSU-A and MHS the

channel T_b is ??:

$$\begin{aligned} T_{b,qv} &= A^2 T_{b,v} + B^2 T_{b,h} \\ T_{b,qh} &= A^2 T_{b,h} + B^2 T_{b,v} \end{aligned} \quad (29)$$

where $T_{b,qv}$ and $T_{b,qh}$ are the quasi-V and quasi-H brightness temperature respectively, and $T_{b,v}$ and $T_{b,h}$ are T_b of the vertical polarization (v-pol) and horizontal (h-pol) respectively. Without any angular offset, there is $A = \cos \phi$ and $B = \sin \phi$ with ϕ as the scan angle.

The equation can be rewritten as a function of twist angles as

$$A = \frac{1}{\sqrt{1 - \sin^2 2\theta \cos^2 \phi}} \cdot [\cos 2\theta \sin \psi - 2 \sin \theta \cos(\phi + \psi) \sin \phi] \quad (30)$$

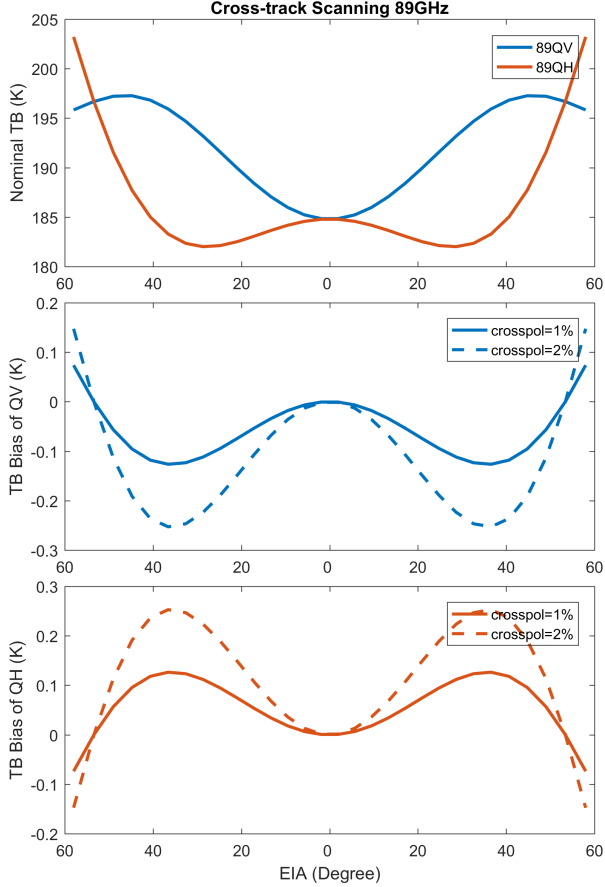


FIG. 5. Effect of cross-pol leakage for cross-track scanning radiometers at 89 GHz of QV and QH. The panels show the (a) nominal TBs, (b) bias at QV, and (c) bias at QH. The RTM simulation assumes mid-latitude winter atmospheric profiles with a SST of 290 K and a wind speed of 5 m/s.

$$\begin{aligned}
 B = & \frac{1}{\sqrt{1 - \sin^2 2\theta \cos^2 \phi}} \\
 & \cdot \{(\cos^2 2\theta + \sin^2 2\theta \sin^2 \phi) \\
 & \cdot [2 \sin^2 \theta \cos(\phi + \psi) \cos \phi - \cos \psi] \\
 & - \frac{1}{2} \sin^2 2\theta \sin 2\phi [2 \sin^2 \theta \cos(\phi + \psi) \sin \phi + \sin \psi] \\
 & - \frac{1}{2} \sin 4\theta \cos \phi \sin 2\theta \cos(\phi + \psi)\}
 \end{aligned} \quad (31)$$

where twist angles include θ of the reflector angle, ψ of the polarization alignment angle, and ϕ of the scan angle. The nominal reflector and polarization alignment angles without offset are $\theta = 45^\circ$ and $\psi = 90^\circ$, and the above two equations reduce to $A = \cos \phi$ and $B = \sin \phi$. The twist angles can be tuned to examine their impact on T_b . We present results in Section III.

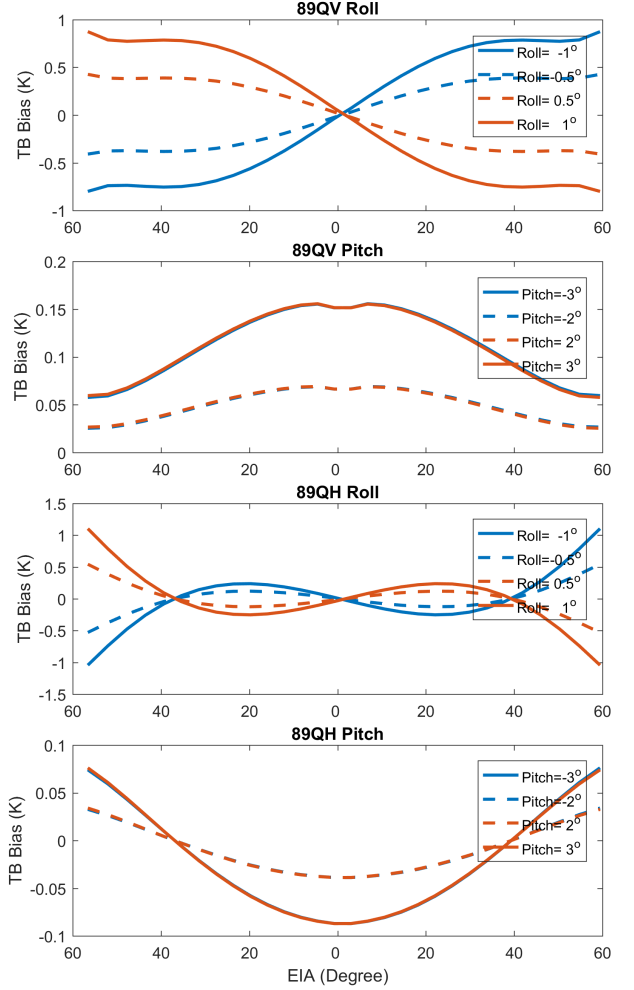


FIG. 6. Attitude biases at 89 GHz QV and QH of cross-track scanning radiometers for (upper two panels) roll and (lower two panels) pitch.

Unlike cross-track scanning, a conical scanning radiometer has constant scan angles. We only consider the offset in the polarization alignment angle ψ , which is the same as in Equation 11.

g. Spacecraft attitude and geolocation

A spacecraft and onboard sensor can have attitude errors in terms of roll, pitch, and yaw. The attitude changes the FOV geolocation and incidence angle and therefore the scene temperature Meissner and Wentz (2006); Kroodsma et al. (2012). Attitude is also linked to other error sources such as Faraday rotation which is dependent on FOV geolocation and angles.

A module is developed for performing coordinate systems and transformation Cai et al. (2011). The steps for coordinate transformation are briefed as follows. The error-free cross-track or conical scanning vector is computed in

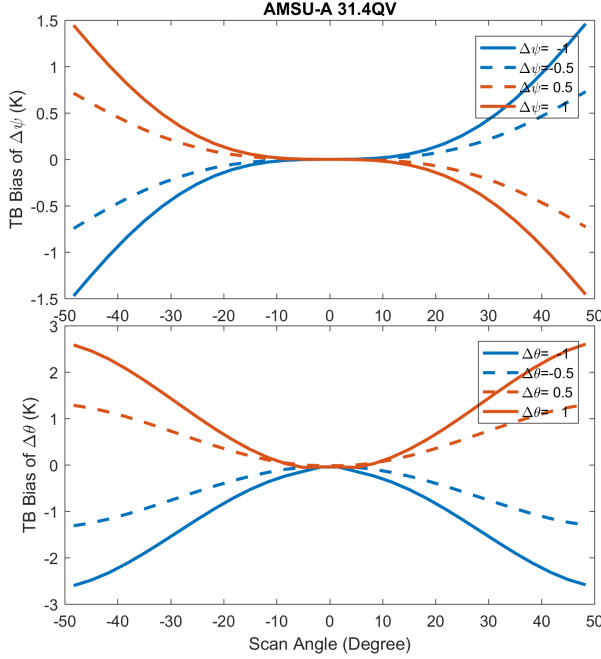


Fig. 7. Sensitivity of twist angle offset for AMSU-A channel-2 of 31.4 GHz QV. a) The sensitivity of polarization alignment angle ψ and b) the sensitivity of reflector angle θ .

the local spacecraft frame of North-East-Down (NED) coordinate. The rotation matrix for the attitude is calculated and applied to the scan vector. The new scan NED vector is transformed to the Earth-centered Earth-fixed (ECEF) geocentric coordinate. The line-of-sight intersection on the ground is computed, and the FOV geolocation is determined. The geodetic coordinate, including FOV geolocation and azimuth and incidence angle, is obtained by transforming the FOV vector from geocentric to geodetic coordinate. The Earth ellipsoid model of WGS-84 is used, while a customized ellipsoid can also be used. The FOV geolocation and angles on the ionosphere shell are computed in the same way but with new ellipsoid parameters counting ionosphere altitude.

The afore-said transforms are from the radiometer to the Earth. It can also be inverted: the input can be realistic FOV geolocations and spacecraft orbit, and the scan NED vector can be determined. Then the attitude can be applied. By doing so, attitude is applied to any operating radiometers. In addition to observational data, the simulator also includes a Keplerian orbit model that simulates a spacecraft orbit Griffin (2004). The orbit can be designed with the six orbit elements. This allows studying attitude in a more idealized but versatile way since the orbit and scan are flexible.

h. Antenna pattern

Antenna pattern determines the weighted radiance a radiometer receives in all solid angles Balanis (2015). APC is necessary in calibration to process weighted T_A to the scene T_b . Antenna pattern can be measured on the ground, and a hybrid one with both measurement and modeling is often used. Errors in the antenna pattern result in T_b bias when there is an overestimate or underestimate of sidelobe and spillover. And the bias is not a constant but dependent on the scene temperature since APC has a scaling effect.

A module is included in the simulator to study the antenna pattern impact. Antenna pattern can be parameterized for the mainlobe, sidelobe, and spillover. The fractions of them can be customized with respect to specific radiometers. Different FOV targets can be set for the mainlobe, sidelobe and spillover. For instance, the nominal operating can be set to have mainlobe and sidelobe viewing the ocean with the cosmic background for spillover. To simulate the deep-space maneuver when the radiometer is flipped upside down, the mainlobe and sidelobe can be set viewing the cosmic with the spillover toward the Earth.

i. Faraday rotation

Faraday rotation takes place when a polarized EM wave goes through the ionosphere with the geomagnetic field ?Meissner and Wentz (2006); Peng et al. (2017). The E-field vector of the EM wave rotates and the Stokes vector is altered. Faraday rotation is dependent on the EM frequency, ionosphere electron content, and the geomagnetic field. It is pronounced at low-frequencies like L-band and for polarimetric radiometers like WindSat where the second and third Stokes are measured. It can be written by ?Meissner and Wentz (2006); Peng et al. (2017)

$$\Omega = \frac{2.365 \cdot 10^2}{f^2} \cdot B \cos \gamma \cdot \text{VTEC} \sec \theta \quad (32)$$

where Ω is in radian, f is the frequency in GHz, B is the geomagnetic field in Tesla, and γ in radian is the angle between the EM wave and B field. VTEC is the integral of vertical total electron content in TECU unit (TECU), where 1 TECU is 10^{16} electron/ m^2 . And θ in radian is the angle between the EM wave and ionosphere.

Faraday rotation can be written in the modified Stokes

$$\begin{bmatrix} T'_v \\ T'_h \\ T'_3 \\ T'_4 \end{bmatrix} = \begin{bmatrix} \cos^2 \Omega & \sin^2 \Omega & 1/2 \sin 2\Omega & 0 \\ \sin^2 \Omega & \cos^2 \Omega & -1/2 \sin 2\Omega & 0 \\ -\sin 2\Omega & \sin 2\Omega & \cos 2\Omega & 0 \\ 0 & 0 & 0 & 1 \end{bmatrix} \begin{bmatrix} T_v \\ T_h \\ T_3 \\ T_4 \end{bmatrix} \quad (33)$$

where the right side Stokes is before entering ionosphere and the left side one is with Faraday rotation effect.

The simulator treats the electron content as a shell from the ground ?Meissner and Wentz (2006); Peng et al. (2017). The altitude of the shell is adjustable and the default setting

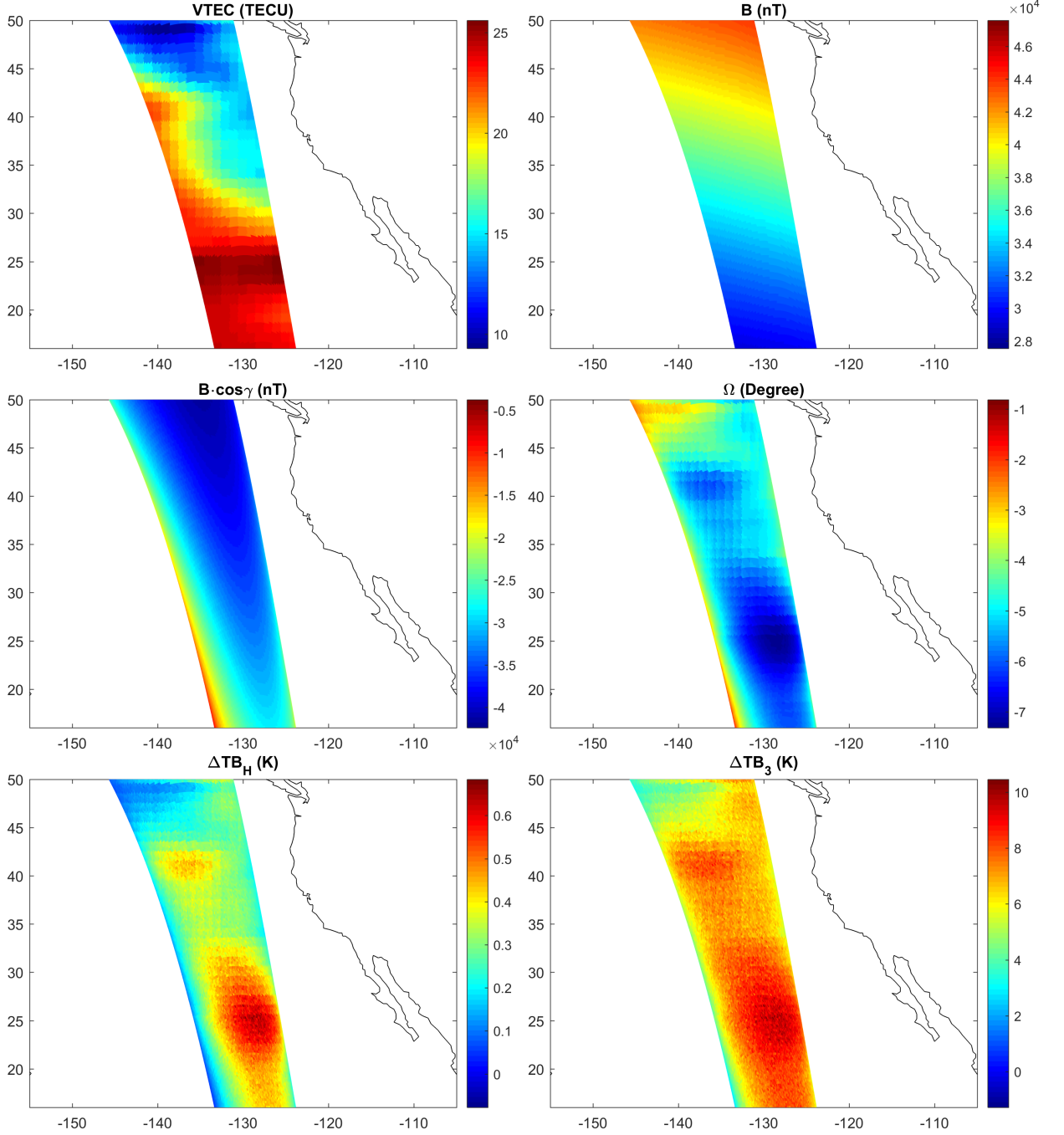


FIG. 8. Channel correlation due to cross-talk. (a) Measured cross-talk of NPP ATMS. (b) simulated cross-talk for ATMS.

is 400 km. The ionosphere altitude can also be varied to account for the fact it has a lower altitude toward the poles. The geolocation of EM waves on the ionosphere is calculated with the Earth mapping module provided the spacecraft orbit and scan geometry. The IGRF model is included as a module for computing the geomagnetic field

Thébault et al. (2015). The total electron content can be obtained from observations or models and imported to the simulator Bilitza et al. (2017).

j. Cross-polarization leakage

The antenna main polarization (co-pol) sees some radiation leakage from the orthogonal polarization plane (cross-pol). The cross-pol leakage can be due to the antenna asymmetry, defects, excitation of higher-order modes Ruf (1998); Davis and Agarwal (2011); Balanis (2016). Cross-pol correction is a necessary step in APC. In the simulator, the cross-pol is a 4×4 matrix as

$$\begin{bmatrix} T'_v \\ T'_h \\ T'_3 \\ T'_4 \end{bmatrix} = \begin{bmatrix} C_{vv} & C_{vh} & C_{v3} & C_{v4} \\ C_{hv} & C_{hh} & C_{h3} & C_{h4} \\ C_{3v} & C_{3h} & C_{33} & C_{34} \\ C_{4v} & C_{4h} & C_{43} & C_{44} \end{bmatrix} \begin{bmatrix} T_v \\ T_h \\ T_3 \\ T_4 \end{bmatrix} \quad (34)$$

where the $C_{i,j}$ is cross-pol coefficients that transforms the cross-pol free Stokes (right) to the new Stokes (left). The values of the coefficients can be customized. In the case of cross-pol free, the matrix is the identity matrix. Examples of cross-pol sensitivity are presented in the results.

k. Reflector emission

An ideal reflector has no self-emission with emissivity equal to zero. In practice, its emissivity can be slightly larger than zero with self-emission seen by the receiver Wentz et al. (2001); Gopalan et al. (2009). The reflector emission introduces errors as it is mixed with radiance of Earth scene, cold and warm references. The emission can be negligible if the emissivity is small enough. An assessment of the reflector emissivity is always necessary.

A module in the simulator is for the reflector emission. It includes the setting for reflector emissivity and physical temperature. The reflector emissivity is dependent on frequency and polarization. For cross-track scanning, the emissivity is dependent on scan angle as it changes in different scan positions. It is insensitive to scan angle for a conical scanning radiometer as the scan angle is very constant. The reflector temperature is dependent on scan and orbit position.

l. Warm load error

Warm load measurements can have errors. The onboard warm load is a blackbody. It is expected that it is a perfect blackbody with emissivity of one. This is opposite to the expectation of the reflector. The emissivity is less than one in practice Twarog et al. (2006); ATB (2016); Alquaied et al. (2018). A correction is needed if the error is large enough. Additionally, the warm load error can come from the temperature gradient, which makes the PRT measured temperature deviate from the actual temperature. The situation can be pronounced when there is a solar intrusion on the warm load target, which induces a large temperature gradient Twarog et al. (2006); ATB (2016); Alquaied et al. (2018).

We provide a module for parameterizing the warm load error. The warm load effective temperature is a function of physical temperature, emissivity, and a bias term. The emissivity multiplied by the physical temperature is the apparent temperature. The emissivity ranges from zero to one. The bias term is a constant, and negative bias means the warm load temperature would be underestimated and positive bias means an overestimate of warm load temperature. The settings are channel dependent.

m. FOV intrusion

FOV intrusion, or beam spoiling, occurs when the antenna FOV is obstructed by objects like the spacecraft or payloads. The effect has been found such as for SSM/I, TMI, AMSU-A Colton and Poe (1999); Wentz et al. (2001); McKague et al. (2010). It is usually obvious at the edge of the scan. The intrusion errors can be parameterized by the temperature of the intrusion object and fraction of intrusion FOV McKague et al. (2010)

$$T_b = T_{b,intr} \Omega_{intr} + T_{b,scene} (1 - \Omega_{intr}) \quad (35)$$

where $T_{b,intr}$ is the brightness temperature of the intrusion object, $T_{b,scene}$ is for the Earth scene, Ω_{intr} is the intrusion solid angle fraction. Ω_{intr} is a function of scan position. Ω_{intr} can be the error function assuming antenna pattern is a Gaussian function. And it can be further simplified as an exponential function when the FOV intrusion is small. $T_{b,intr}$ can be set as a function of both cross-track and along-track scan.

n. Bandpass spectral response

The spectral response is the bandpass responsivity of the finite bandwidth around the center frequency Kim et al. (2014); ATB (2016). The spectral response includes the response of amplifiers and BPFs and is dependent on the hardware. It usually exhibits channel-dependent responsivity that appears irregular than a flat spectrum. It is often measured in prelaunch tests. The effective channel radiance is the incoming radiance weighted by the spectral response.

The spectral response can be counted in the simulator. The channel bandpass can be split to plenty of sub-frequencies. A channel can have double sidebands or more subbands. RTM simulation is performed at every sub-frequency, and the channel effective brightness temperature is the convolution of T_b with the spectral response.

$$T_{b,chan} = \sum_{i=1}^n \int_{f_i - B_i/2}^{f_i + B_i/2} T_b(f) S_i(f) df \quad (36)$$

where $T_{b,chan}$ is the channel effective brightness temperature, f is the sub-frequency, i is number of subband, f_i is the subband center frequency, B is the subband bandwidth, $S_i(f)$ is the subband spectral response.

Doing so enables more accurate RTM simulations Yang and Yang (2018), since the atmospheric absorption is usually nonlinear in the finite bandpass. When the spectral response or atmospheric absorption nonlinearity is pronounced, a noticeable difference can be found between accurate simulation across the bandwidth and at only the center frequency of a channel.

o. Interference of instrumental and geomagnetic field

Interference can take place due to the onboard instrument. For example, in the early flight phase of GMI, instrumental induced magnetic biases are found in all channels. The 10.65 GHz channel has a pronounced bias of 1.2 K of peak-to-peak. The bias is scan-dependent but is time invariant. The cause was later identified as instrumental interference of the reflector spin and feed switches on the launch restraints Draper et al. (2015); Wentz and Draper (2016). The variation of the geomagnetic field was also found to affect the radiometer. In our simulator, we consider the instrumental bias as an additive signal that is channel dependent. The additive bias can be customized and is added to T_A .

2. Observation operator error

a. Ancillary models and modules

A 1-D RTM is included in the simulator Yang et al. (2016); Yang and Yang (2018). The atmospheric gaseous absorption is based on the Rosenkranz model Rosenkranz (2017); Rosenkranz and Cimini (2019). An oceanic emission model is included ?. The users can also choose other surface and atmospheric absorption model and import the computed variables to the simulator.

The IGRF model is included for computing the geomagnetic field. It is the 12th generation of the model that covers from 1990 to the end of 2019 Thébaud et al. (2015). It is a series of models describing the geomagnetic field and is published by the International Association of Geomagnetism and Aeronomy (IAGA). The geomagnetic field is derived as the gradient of the magnetic scalar potential. The input for IGRF is geodetic coordinates, and the output is the vector of the geomagnetic field. Our simulator can also import and use geomagnetic fields produced by other models.

A Keplerian orbit model is used for simulating the spacecraft orbit Griffin (2004). The input is the six orbit elements, and the output is the spacecraft geolocation. Orbital perturbations are not considered in the model, but it is sufficient to study effects like spacecraft attitude. Observational orbits can be imported to the simulator.

3. Representativeness error

4. Pre-processing error

Acknowledgments. Keep acknowledgments

Data availability statement. The data availability statement is where authors should describe how the data underlying the findings within the article can be accessed and reused. Authors should attempt to provide unrestricted access to all data and materials underlying reported findings. If data access is restricted, authors must mention this in the statement.

References

- , 2016: Nasa global precipitation measurement (gpm) microwave imager (gmi) level 1b (11b). *Algorithm Theoretical Basis Document (ATBD)*.
- Alquaied, F., R. Chen, and W. L. Jones, 2018: Hot load temperature correction for trmm microwave imager in the legacy brightness temperature. *IEEE Journal of Selected Topics in Applied Earth Observations and Remote Sensing*, **11** (6), 1923–1931.
- Balanis, C., 2016: *Antenna theory: Analysis and design*, 318. John Wiley & Sons, Hoboken, New Jersey.
- Balanis, C. A., 2015: *Antenna theory: analysis and design*. John Wiley & sons.
- Bilitza, D., D. Altadill, V. Truhlik, V. Shubin, I. Galkin, B. Reinisch, and X. Huang, 2017: International reference ionosphere 2016: From ionospheric climate to real-time weather predictions. *Space weather*, **15** (2), 418–429.
- Cai, G., B. M. Chen, and T. H. Lee, 2011: *Unmanned rotorcraft systems*. Springer Science & Business Media.
- Colton, M. C., and G. A. Poe, 1999: Intersensor calibration of dmsp ssm/i's: F-8 to f-14, 1987-1997. *IEEE Transactions on Geoscience and Remote Sensing*, **37** (1), 418–439.
- Davis, W. A., and K. K. Agarwal, 2011: *Radio Frequency Circuit Design*. 2nd ed., Wiley, New York, doi:10.1002/0471200689.
- Draper, D. W., D. A. Newell, F. J. Wentz, S. Krimchansky, and G. M. Skofronick-Jackson, 2015: The global precipitation measurement (gpm) microwave imager (gmi): Instrument overview and early on-orbit performance. *IEEE Journal of Selected Topics in Applied Earth Observations and Remote Sensing*, **8** (7), 3452–3462.
- Gopalan, K., W. L. Jones, S. Biswas, S. Bilanow, T. Wilheit, and T. Kasparis, 2009: A time-varying radiometric bias correction for the trmm microwave imager. *IEEE transactions on geoscience and remote sensing*, **47** (11), 3722–3730.
- Griffin, M. D., 2004: *Space vehicle design*. AIAA.
- Kim, E., C.-H. J. Lyu, K. Anderson, R. Vincent Leslie, and W. J. Blackwell, 2014: S-npp atms instrument prelaunch and on-orbit performance evaluation. *Journal of Geophysical Research: Atmospheres*, **119** (9), 5653–5670.
- Kroodsma, R. A., D. S. McKague, and C. S. Ruf, 2012: Inter-calibration of microwave radiometers using the vicarious cold calibration double difference method. *IEEE Journal of Selected Topics in Applied Earth Observations and Remote Sensing*, **5** (3), 1006–1013.

- Kuan, D. T., A. A. Sawchuk, T. C. Strand, and P. Chavel, 1985: Adaptive noise smoothing filter for images with signal-dependent noise. *IEEE transactions on pattern analysis and machine intelligence*, **(2)**, 165–177.
- Lee, T. H., 2004: *The Design of CMOS Radio-Frequency Integrated Circuits*. Cambridge Univ, doi:10.1017/cbo9780511817281.
- Matsumoto, M., and T. Nishimura, 1998: Mersenne twister: a 623-dimensionally equidistributed uniform pseudo-random number generator. *ACM Transactions on Modeling and Computer Simulation (TOMACS)*, **8 (1)**, 3–30.
- McKague, D. S., C. S. Ruf, and J. J. Puckett, 2010: Beam spoiling correction for spaceborne microwave radiometers using the two-point vicarious calibration method. *IEEE transactions on geoscience and remote sensing*, **49 (1)**, 21–27.
- Meissner, T., and F. J. Wentz, 2006: Polarization rotation and the third stokes parameter: The effects of spacecraft attitude and faraday rotation. *IEEE Transactions on Geoscience and Remote Sensing*, **44 (3)**, 506–515.
- Mo, T., 1996: Prelaunch calibration of the advanced microwave sounding unit-A for NOAA-K. *IEEE Transactions on Microwave theory and Techniques*, **44 (8)**, 1460–1469.
- Peng, J., and Coauthors, 2017: Soil moisture active/passive l-band microwave radiometer postlaunch calibration. *IEEE Transactions on Geoscience and Remote Sensing*, **55 (9)**, 5339–5354.
- Riley, W. J., 2008: Nist special publication 1065. *Handbook of frequency stability analysis*, 60.
- Robel, J., and A. Graumann, 2014: Noaa klm user’s guide with noaa-n. *N Prime, and MetOp SUPPLEMEN*: https://www.nasa.gov/pdf/111742main_noaa_n_booklet.pdf.
- Rosenkranz, P., 2017: Line-by-line microwave radiative transfer (non-scattering). *Remote Sensing Code Library*, <https://doi.org/10.21982/M,81013>.
- Rosenkranz, P. W., and D. Cimini, 2019: Speed dependence of 22-and 118-ghz line shapes for tropospheric remote sensing. *IEEE Transactions on Geoscience and Remote Sensing*, **57 (12)**, 9702–9708.
- Ruf, C. S., 1998: Constraints on the polarization purity of a stokes microwave radiometer. *Radio Science*, **33 (6)**, 1617–1639.
- Schiek, B., H.-J. Siweris, and I. Rolfes, 2006: *Noise in high-frequency circuits and oscillators*. John Wiley & Sons.
- Sullivan, D. B., D. W. Allan, D. A. Howe, and F. L. Walls, 1990: *Characterization of clocks and oscillators*. National Institute of Standards and Technology Technical Note.
- Thébault, E., and Coauthors, 2015: International geomagnetic reference field: the 12th generation. *Earth, Planets and Space*, **67 (1)**, 1–19.
- Twarog, E. M., W. E. Purdy, P. W. Gaiser, K. H. Cheung, and B. E. Kelm, 2006: Windsat on-orbit warm load calibration. *IEEE Transactions on Geoscience and Remote Sensing*, **44 (3)**, 516–529.
- Ulaby, F. T., and Coauthors, 2014: *Microwave radar and radiometric remote sensing*, Vol. 4. University of Michigan Press Ann Arbor.
- Vasilescu, G., 2005: *Electronic noise and interfering signals: principles and applications*. Springer Science & Business Media.
- Weng, F., and Coauthors, 2013: Calibration of suomi national polar-orbiting partnership advanced technology microwave sounder. *Journal of Geophysical Research: Atmospheres*, **118 (19)**, 11–187.
- Wentz, F. J., P. Ashcroft, and C. Gentemann, 2001: Post-launch calibration of the trmm microwave imager. *IEEE Transactions on Geoscience and Remote Sensing*, **39 (2)**, 415–422.
- Wentz, F. J., and D. Draper, 2016: On-orbit absolute calibration of the global precipitation measurement microwave imager. *Journal of Atmospheric and Oceanic Technology*, **33 (7)**, 1393–1412.
- Yang, J. X., D. S. McKague, and C. S. Ruf, 2016: Uncertainties in radiometer intercalibration associated with variability in geophysical parameters. *Journal of Geophysical Research: Atmospheres*, **121 (19)**, 11–348.
- Yang, J. X., and H. Yang, 2018: Radiometry calibration with high-resolution profiles of gpm: Application to atms 183-ghz water vapor channels and comparison against reanalysis profiles. *IEEE Transactions on Geoscience and Remote Sensing*, **57 (2)**, 829–838.